Accepted 16 July, 2024

ORIGINAL ARTICLE

Mountain waves developing inside and aloft stably stratified turbulent boundary layers

Lucile Pauget[1,2†] | Francois Lott[1*] | Christophe Millet[2‡]

[1]Universite PSL, Ecole Normale Supérieure, Département des géosciences, Laboratoire de Météorologie Dynamique, Paris France

[2]Commissariat à l'Energie atomique/DAM, Bruyères le Chatel, France

Correspondence
Francois Lott, Laboratoire de Météorologie Dynamique, Ecole Normale Supérieure, 24 rue Lhomond, 75231 Paris France
Email: flott@lmd.ens.fr

Funding information
VESRI Schmidt Future project DataWave; Laboratoire de Recherche Conventionné "Yves Rocard," a collaborative unit between CEA and ENS.

A linear theory of the trapped mountain waves that develop in a turbulent boundary layer is presented. The theory uses a mixing length turbulence model based on Monin-Obukhov similarity theory. First, the backward reflection of a stationary gravity wave (GW) propagating toward the ground is examined. Three parameters are investigated systematically: the Monin-Obukhov length (L_{mo}), the roughness length (z_0) and the limit value of the mixing length (λ) aloft the "inner" layer. The reflection coefficient appears to strongly depends on the Richardson number aloft the inner layer ($J = \frac{\lambda}{\kappa L_{mo}}$, with κ the von-Karman constant): the reflection decreasing when the stability (J) increases. The influence of the roughness and mixing lengths on the reflection is explained in terms of the depth of a "pseudo"-critical level located below the surface: the reflection decreasing when the depth of the "pseudo" critical level decreases. The preferential modes of oscillations occurring in presence of mountain forcing are then analysed, the decay rate of the trapped waves downstream increasing when the reflection decreases. At a certain point nevertheless, when the absorption is large but the boundary layer depth deep enough, there appears trapped modes that interact little with the surface.

[*]Conceptualization, Formal analysis, Methodology, Writing
[†]Formal analysis, Methodology, Writing
[‡]Methodology, Writing

KEYWORDS
Trapped mountain waves, Neutral and stratified boundary layers, Turbulence

1 | INTRODUCTION

An early theory for gravity waves developing in the lee of mountain ranges was proposed by Scorer (1949) who demonstrated that resonant modes can be excited by mountains when the background wind and stratification vary with altitude. More specifically and in the 2D-case, they occur when the Scorer parameter,

$$S(z) = \frac{N^2}{U^2} - \frac{U_{zz}}{U}, \tag{1}$$

decreases with altitude above the surface. Here N, U and z are the background buoyancy frequency, the background wind and the altitude, respectively. In this case all the harmonics with horizontal wavenumber k that encounter a turning point h_t where

$$S(h_t(k)) = k^2, \tag{2}$$

are trapped at low levels. A discrete number of them become resonant in the inviscid case, as a result of successive reflections between their turning level and the surface. While Scorer (1949), and more recently Teixeira et al. (2013), applied the theory to a two layer atmosphere, cases with smooth variations of $S(z)$ have also been analyzed in numerous studies (see for instance Durran (1986) or Wurtele et al. (1996)). Of particular interest to our study is that of Keller (1994) which includes trapped waves with strong increase of the wind above the surface. Nevertheless and after Scorer (1949), it has been realized that trapped waves can also appear at a sharp density or wind inversion, in which case the interaction with the surface is not as pronounced as when the waves result from multiple reflections between the surface and turning levels (Vosper, 2004; Sachsperger et al., 2017). In the present paper, we will see that near resonant modes that have slight interaction with the surface can also be found when the background atmospheric state varies smoothly in the vertical.

If we now return to the initial Scorer (1949)'s theory, one of its weaknesses is that it neglects the dissipative effects occurring within the boundary layer, regardless that the variations with altitude of wind and stratification occurring in the boundary layer are potentially ducting trapped lee waves. This neglect of dissipation yields to overestimate mountain waves amplitude, downslope winds and trapped waves downstream development, as revealed modelling studies (Richard et al., 1989; Miller and Durran, 1991; Georgelin et al., 1994). More recently, Jansing et al. (2022) and Tian et al. (2023) demonstrated that simulations of mountain waves and Foehn strongly depends on the boundary layer parameterizations, parameterizations that are still uncertain in mountainous area (Goger et al., 2019) (see also the review in Serafin et al. (2018)). For completeness note that other deficiencies concerning boundary layer effects over complex terrain are discussed in Tsiringakis et al. (2017), Lehner and Rotach (2018) and Vosper et al. (2018).

Beyond numerical models, attempts to understand the more fundamental mechanism at works in the interaction between the trapped lee waves and the boundary layer were motivated by observations. During the Mesoscale Alpine Program (Bougeault et al., 2001), Smith et al. (2002) noticed that a strong absorption by a near stagnant surface layer could inhibit the development of trapped waves, despite favorable conditions aloft. In subsequent papers, they proposed to analyse systematically the absorptive properties of the surface, illustrating that the combination of reduced winds in the boundary layer and dissipation contribute to the absorption (Smith et al., 2006). They characterized a surface reflection coefficient for waves returning to the surface downstream and related it to the spatial decay rate of trapped waves (referred to as q and α respectively). In short, a small reflection is associated with a strong decay.

Nevertheless, in Smith et al. (2006) but also in Jiang et al. (2006), frictional effects are represented by bulk formula with linear Rayleigh drag, which are not extensively used in models. Indeed the dissipative effects are more often taken into account by introducing turbulence closures based on eddy diffusivity. A fundamental difficulty when using such closures is that the equations have higher order derivative in the vertical (6 compared to 2 for the inviscid Taylor Goldstein equation). In the constant eddy viscosity case, Lott (2007) obtained solutions by using asymptotic techniques where the flow is split into an outer region, where viscosity is negligible, and an inner region, where dissipative effects compare to disturbance advection (Jackson and Hunt, 1975). This region has depth varying according to an "inner layer" scale h_i that is distinct from the boundary layer depth, and satisfying

$$kU(h_i(k)) \approx \frac{\nu'}{h_i^2}, \tag{3}$$

where ν' is the eddy diffusivity acting on the disturbance produced by the mountain. An important result is that when the Richardson number near the surface

$$Ri(z) = \frac{N^2}{U_z^2} \underbrace{\approx}_{z \to 0} J > 0.25, \tag{4}$$

increases, the surface reflection decreases even in the inviscid limit. Furthermore, in the inviscid limit the reflection is almost total when $J < 0.25$. This condition is similar to the Richardson-number instability criterion for continuously stratified inviscid parallel flows (Miles, 1961; Howard, 1961). Elaborating on this further, Lott (2007) showed that the neutral modes of Kelvin-Helmholtz instability (Drazin, 1958) can also correspond to trapped lee waves (see also Soufflet et al. (2022)).

A limit of the constant eddy viscosity case is that in reality, turbulent viscosity over a rough surface is more realistically represented using mixing-length theory, the mixing length decreasing when approaching the surface. This introduces other difficulties, for instance one needs to treat the problem using curvilinear coordinates and re-calculate the viscous solutions. To a certain extent, this was accomplished in the past, quite theoretically in Belcher et al. (1993), Belcher and Wood (1996), and Hunt et al. (1988), and more numerically in Weng et al. (1997). However in these papers the trapping of the waves between the surface (or the top of the inner layer) and the turning levels was not fully considered. Specifically, the authors did not capture trapped wave dissipation that may occur in atmospheric boundary layers. In a recent paper, Lott et al. (2023) derived such a theory (hereinafter referred to Part 1), and focused on the nature of the transition from form drag to wave drag, and from downstream sheltering to upstream blocking. During the transition, which is shown to occur when the Richardson number value aloft the surface layer J is close to 1, it was noticed that trapped waves deeply affect the dynamics. It was also noticed that for small J the turning levels are too close to the surface for trapped modes to emerge, and that for large J the surface absorption is too large for trapped modes to develop horizontally. Lott et al. (2023) also describe briefly the sensitivity to the Froude number,

$$F = \frac{U(\infty)}{N(\infty)L}, \tag{5}$$

where L is a characteristic length of the mountain. This number controls the significance of the non-hydrostatic effects (Yu and Teixeira, 2014). The purpose of the present paper is to assess further these issues, first by calculating the reflection coefficient and second by trying to relate the flow response to a mountain forcing in terms of this reflection coefficient. As we shall see, the decay rate of the trapped waves is well explained by the absorptive properties of the surface and their horizontal wavenumber is quite controlled by the more conventional inviscid trapped wave dynamics.

The plan of the paper is as follows. Section 2 recalls aspects of the formalism used in Part I and needed here. Section 3 evaluates the reflection coefficients. Section 4 analyses the response of the flow to an idealized mountain using the full model presented in Part I, with a focus on the spatial decay rate of trapped modes. Section 5 concludes and the appendix gives solutions to the homogeneous inviscid problem that were not given in Part I and that are required to evaluate the surface reflection coefficients.

2 | TURBULENCE CLOSURE AND BACKGROUND FLOW PROPERTIES

Although the evaluation of solutions in the presence of a mountain necessitates curved coordinates, they are not needed to calculate surface reflection downstream so we will lighten the formalism and consider cartesian coordinate (x, z) in the following. For completeness, we recall here that as in part I, the vertical fluxes of horizontal momentum and buoyancy are parameterized by an eddy diffusivity ν based on mixing length theory,

$$\tau_{xz} = \nu \partial_z u, q_z = \nu \partial_z b, \quad \nu = \Lambda_0^2 \left\| \frac{\partial u}{\partial z} \right\|, \tag{6}$$

where u is the zonal wind and $b = -g\frac{\theta - \theta_s}{\theta_s}$ is the buoyancy, θ being potential temperature and θ_s a reference value. For simplicity, we slightly modify the Blackadar formulation for the mixing length - common for neutral flows - but keep the same asymptotes,

$$\Lambda_0 = \lambda \tanh\left(\kappa \frac{z + z_0}{\lambda}\right), \tag{7}$$

where z_0, κ, and λ are the roughness length, the von Karman constant, and the limit value of the mixing length respectively. The formulation for the mixing length in (7) gives background wind and buoyancy profiles with uniform fluxes,

$$U_V(z) = \frac{u_*}{\kappa} \ln\left(\frac{\sinh(\kappa \frac{z+z_0}{\lambda})}{\sinh(\kappa \frac{z_0}{\lambda})}\right), \qquad B_V(z) = \frac{b_*}{\kappa} \ln\left(\frac{\sinh(\kappa \frac{z+z_0}{\lambda})}{\sinh(\kappa \frac{z_0}{\lambda})}\right), \tag{8}$$

where $u_* = \sqrt{\tau_s/\rho_s}$ is the friction velocity, and $b_* = g\, H_s/(\rho_s c_p u_* \theta_s)$ is the buoyancy scale, with τ_s and H_s for surface stress and heat flux and c_p for the air heat capacity per unit mass at constant pressure. The background wind in (8) is going to infinity when $z \to \infty$, which makes that the Scorer parameter in (1) goes to zero: all the harmonics are trapped which is not representative of the real atmosphere. For this reason, we also considered cases where the background wind smoothly becomes constant beyond a boundary layer depth d writing

$$U(z) = \frac{u_* d}{\lambda} \tanh\left[\frac{\lambda}{u_* d} U_V(z)\right], B(z) = B_V(z), \tag{9}$$

keeping in mind that in the limit $d \to \infty$ U and U_v coincide.

Figure 1a shows the wind profile in (9) for $d = \infty$ and $d = 1km$ and for the same parameter values as in Fig. 1 in Part I. When $d = \infty$ the wind shear is almost constant everywhere whereas it is approximately constant below

300m typically when $d = 1$km (see zoom in Fig.1b). The zoom also shows that near the surface, the profiles acquire a log character, as expected. Figure 1b, also shows the location of the inner layer, evaluated for the case where the mountain has a characteristic length $L = 1$km (i.e. $h_i(1/L)$ according to Eq. 3, and anticipating for ν' the values given in (16a). Figures 1b) and 1c) also show the linear asymptote of U and B when $\lambda \ll z \ll d$, illustrating that

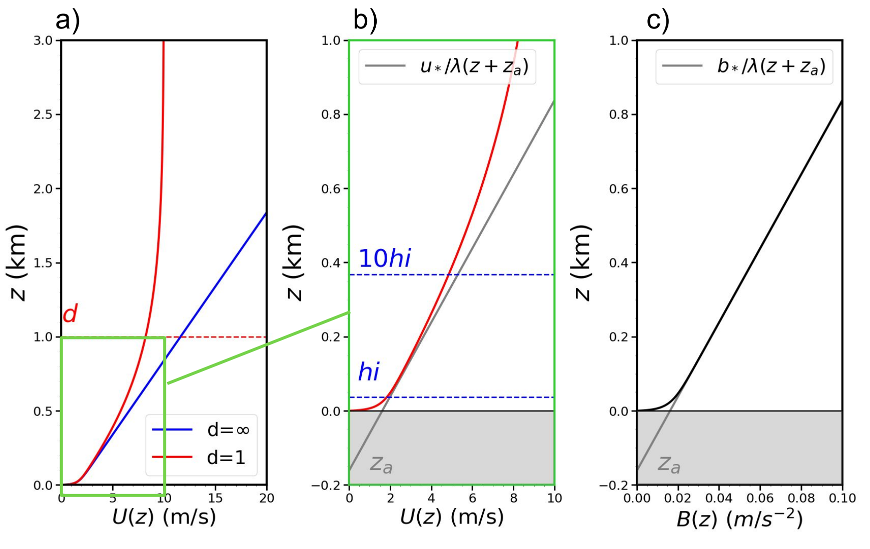

FIGURE 1 Background profiles for z_0=1m, λ=20m, u_* = 0.2 m/s, b_*= 5 m/s^{-2}, d = 1km, L = 1km: a) Background wind U in the constant shear case (blue, see (8)) and the variable shear case (red, see (9). b) Zoom for the wind profile in the boundary layer and in grey its linear asymptote in (10). Are also shown the depth "critical level" depth z_a and the inner layer scale $h_i(1/L)$. c) Buoyancy profile and its linear fit.

$$U(z) \underbrace{\approx}_{\lambda \ll z \ll d} \frac{u_*(z+z_a)}{\lambda}, \quad B(z) \underbrace{\approx}_{\lambda \ll z} \frac{b_*(z+z_a)}{\lambda} \tag{10}$$

where the parameter,

$$z_a = z_0 - \frac{\lambda}{\kappa} \log\left(2\sinh\frac{\kappa z_0}{\lambda}\right). \tag{11}$$

At least in the boundary layer and above the inner layer, Figs. 1b)-1c) show that these asymptotes approximate U and B in (9) quite well. As we shall see, the parameter z_a can be viewed as the critical level depth for the inviscid part of the response.

As said in the introduction, an important parameter of the flow is the Richardson number (4), for the boundary layer profiles in (9)

$$Ri(z) = \frac{N^2}{U_z^2} \approx \begin{cases} 0 & \text{for} \quad z \to 0 \\ J = \frac{b_* \lambda}{u_*^2} = \frac{\lambda}{\kappa L_{mo}} & \text{for} \quad \lambda << z << d \\ \infty & \text{for} \quad d << z \end{cases} \tag{12}$$

where $N^2 = B_z$ and L_{mo} is the Monin-Obukhov length. Still for the boundary layer flow (9) the Froude number (5)

$$F = \frac{U(\infty)}{N(\infty)L} = \sqrt{\frac{u_*^2}{b_* \lambda}} \frac{d}{L} = J^{-1/2} \frac{d}{L}. \tag{13}$$

A difficulty is that F changes when J changes. In the present paper, as we are focused on the absorbing properties of the boundary layer we make the choice to systematically vary the dissipative parameters λ and z_0 and the parameter J, F will in most cases take the two contrasting values $F = 1, \infty$ ($d = \sqrt{J} L, \infty$). In these two cases, the fraction of harmonics that stay trapped compared to the number of harmonics excited by the mountain remains constant when the other parameters change. Note nevertheless that to keep F constant we are forced to increase the shear layer depth d when J increases. J will therefore have two contrasting effect: on the one hand trapped lee waves will be more attenuated at the surface when J increases, but on the other the ducting region will increase enabling more modes to develop. We will see that some of them interact little with the surface and can propagate downstream substantially even when surface absorption is large.

3 | LINEAR SOLUTIONS

To analyse the gravity wave absorption at the surface, we use the boussinesq equations linearized around U and B, and evaluate the behaviour of harmonics with wavenumber $k > 0$, i.e. considering disturbance fields under the form

$$\left(u', w', p', b'\right) = \left(\mathbf{u}, \mathbf{w}, \rho_s \mathbf{p}, \mathbf{b}\right) e^{ikx}, \tag{14}$$

where u', and w', are horizontal and vertical wind disturbances, whereas p' and b' are disturbances in pressure and buoyancy and ρ_s a reference density. In this Fourier space, the equations we solve are

$$ikU\mathbf{u} + \mathbf{w}\partial_z U + ik\mathbf{p} = \partial_z 2\Lambda_0 u_* \partial_z \mathbf{u}, \tag{15a}$$

$$ikU\mathbf{b} + N^2\mathbf{w} = \partial_z \Lambda_0 \left(u_* \partial_z \mathbf{b} + b_* \partial_z \mathbf{u}\right), \tag{15b}$$

$$ikU\mathbf{w} + \partial_z \mathbf{p} - \mathbf{b} = 0, \tag{15c}$$

$$ik\mathbf{u} + \partial_z \mathbf{w} = 0, \tag{15d}$$

which are the dimensional form of the homogeneous part of Eq. 29 in Part I, the dissipation being neglected in (15c) consistent with the Prandtl approximation. Also, the dissipative terms in (15a) and (15b) result from the linearizations

$$\Lambda_0^2 \left\| \frac{\partial u}{\partial z} \right\| \frac{\partial u}{\partial z} \approx \Lambda_0^2 \left(\frac{dU}{dz} \right)^2 + 2\Lambda_0^2 \left(\frac{dU}{dz} \right) \frac{\partial u'}{\partial z} = u_*^2 + \underbrace{2\Lambda_0 u_*}_{\nu'} \frac{\partial u'}{\partial z}, \tag{16a}$$

$$\Lambda_0^2 \left\| \frac{\partial u}{\partial z} \right\| \frac{\partial b}{\partial z} \approx u_* b_* + \Lambda_0 \left(u_* \partial_z b' + b_* \partial_z u' \right), \tag{16b}$$

respectively.

3.1 | Outer solution

The scale analysis of the various terms in Eqs. 15 have been done systematically in Part I and for the case where the limit value of the mixing length is much smaller than the characteristic horizontal scale of the waves $\lambda << L$. In this case it was shown that all dissipative terms on the RHS of (15) are small and can be neglected at the leading order. This simplification does not allow to satisfy all the boundary conditions and can only be applied in an "outer region" defined by $z >> h_i$. After verification that $h_i > \lambda$ in the cases we consider, in this outer region the background wind and stratification can be approximated by,

$$U \approx \frac{u_* d}{\lambda} \tanh \left(\frac{z + z_a}{d} \right), \; N^2 \approx \frac{b_*}{\lambda}. \tag{17}$$

With these simplified form, the "outer solutions" in the constant shear case $d = \infty$, are expressed in terms of Hankel functions whereas in the variable shear case solutions are expressed in terms of hypergeometric functions all of them exhibiting a critical level at $-z_a$ (i.e below the surface, see appendix for details). What is important is that in all cases we can use analytical solutions with asymptotic behaviours,

$$\mathbf{w}_I(z) \underbrace{\approx}_{z/L \to \infty} e^{-m(z+z_a)}, \; \mathbf{w}_D(z) \underbrace{\approx}_{z/L \to \infty} e^{+m(z+z_a)} \tag{18a}$$

$$\mathbf{w}_I(\bar{z}) \underbrace{\approx}_{z/L \to 0} a_1 \left(z + z_a \right)^{1/2+i\mu} + a_2 \left(z + z_a \right)^{1/2-i\mu},$$

$$\mathbf{w}_D(z) \underbrace{\approx}_{z/L \to 0} a_3 \left(z + z_a \right)^{1/2+i\mu} + a_4 \left(z + z_a \right)^{1/2-i\mu}, \tag{18b}$$

with more details in the appendix. In (18a) and (18b),

$$m = \sqrt{|k^2 - F^{-2} L^{-2}|}, \text{ and } \mu = \sqrt{|J - \frac{1}{4}|}, \tag{19}$$

$\lambda(m)$ \ $z_0(m)$	0.5	1	2
5	32	24	16
20	196	162	128
50	604	518	432

$\lambda(m)$ \ $z_0(m)$	0.5	1	2
5	22 (29)	23 (29)	24 (29)
20	36 (73)	40 (73)	43 (73)
50	50 (135)	52 (135)	57 (135)

TABLE 1 Values of z_a (left) and of $h_i(1/L)$ ($\delta(1/L)$) (right) for different values of λ and z_0 (see Eqs. (11), (3) with ν' in (16a) and (21))

respectively, μ being changed in $i\mu$ when $J < 1/4$ and m in $-im$ when $k^2 < F^{-2}L^{-2}$. With these conventions, $\mathbf{w}_I$ exponentially decays as z increases or is an upward propagating wave when m is imaginary, whereas $\mathbf{w}_D$ grows as z increases or is a downward propagating gravity wave.

As we shall see and to calculate surface reflections when $J < 0.25$ we will need to analyse the outer solutions in the far field and in the variable shear case rather than just above the inner layer. In this case and to "de-activate" the ducting region we will use hydrostatic solutions. In the outer region this is simply done by changing m in (19) by

$$m = -\frac{i}{FL}: \tag{20}$$

there is no turning levels and trapped harmonics. For completeness, note that the hydrostatic approximation is always made in the very thin inner region.

3.2 | Inner solution

To find solutions that match the outer solution and satisfy the 3 surface boundary conditions on the wind $(\mathbf{u}, \mathbf{w})$ and buoyancy $\mathbf{b}$ we evaluated numerically in Part I 4 solutions of the inner equations. Note nevertheless that for mathematical convenience, the inner equations we derive do not use vertical distances scaled by the inner scale h_i but by the scale

$$\delta(k) = \left(\frac{\lambda^2}{k}\right)^{1/3}. \tag{21}$$

We have verified that in all cases we analyse the two scales compare in amplitude h_i always being $1-3$ times smaller than δ (see table 1). Beyond this technical issue, the most important result is that near aloft the inner layer, the background wind shear is almost constant and the 4 inner solutions needed have asymptotic behaviour

$$\mathbf{w}_{v1} \underbrace{\approx}_{z/\delta\to\infty} (z+z_a)^{1/2-i\mu},\ \mathbf{w}_{v2} \underbrace{\approx}_{z/\delta\to\infty} (z+z_a)^{1/2+i\mu}, \tag{22a}$$

$$\mathbf{w}_{v3} \underbrace{\approx}_{z/\delta\to\infty} (z+z_a)^{-\frac{9+2J}{4}}\, e^{-\frac{2}{3}\sqrt{i}\left(\frac{z+z_a}{\delta}\right)^{3/2}}, \mathbf{w}_{v4} \underbrace{\approx}_{z/\delta\to\infty} (z+z_a)^{-\frac{5-2J}{4}}\, e^{-\frac{2}{3}\sqrt{\frac{i}{2}}\left(\frac{z+z_a}{\delta}\right)^{3/2}}. \tag{22b}$$

The interest here is that when $J > 0.25$, we know from Booker and Bretherton (1967), that the asymptotic behaviour of $\mathbf{w}_{v1}$ in (22a) corresponds to that of a downward propagating wave and that of $\mathbf{w}_{v2}$ to an upward propagating wave (in the convention $k > 0$). When $J < 0.25$, the two solutions need to be combined to build vertically propagating disturbances which complicates the analysis (see next section). Finally, $\mathbf{w}_{v3}$ and $\mathbf{w}_{v4}$ decay exponentially when z increases, they are entirely "dissipative" solutions as indicate their exponential decay rate scaled by the inner layer scale δ.

4 | ABSORPTION BY THE SURFACE LAYER

The absorbing properties of the surface can be estimated using the solution above the inner layer. Following Lott (2007), the solution can be expressed as the superposition of the four viscous solutions with asymptotic behaviour given in (22), i.e.

$$\mathbf{w} = \mathbf{w}_{v1} + R\mathbf{w}_{v2} + c\mathbf{w}_{v3} + d\mathbf{w}_{v4}, \tag{23}$$

with similar expressions for the horizontal wind and buoyancy. From the numerical integration of the four viscous solutions to the surface described in Part I we then evaluate the coefficients R, c, and d so as to satisfy the three surface boundary conditions,

$$\mathbf{w}(z=0) = \mathbf{u}(z=0) = \mathbf{b}(z=0) = 0, \tag{24}$$

while imposing "unit" amplitude upward propagating solution ($\mathbf{w}_{v1}$ see (23)).

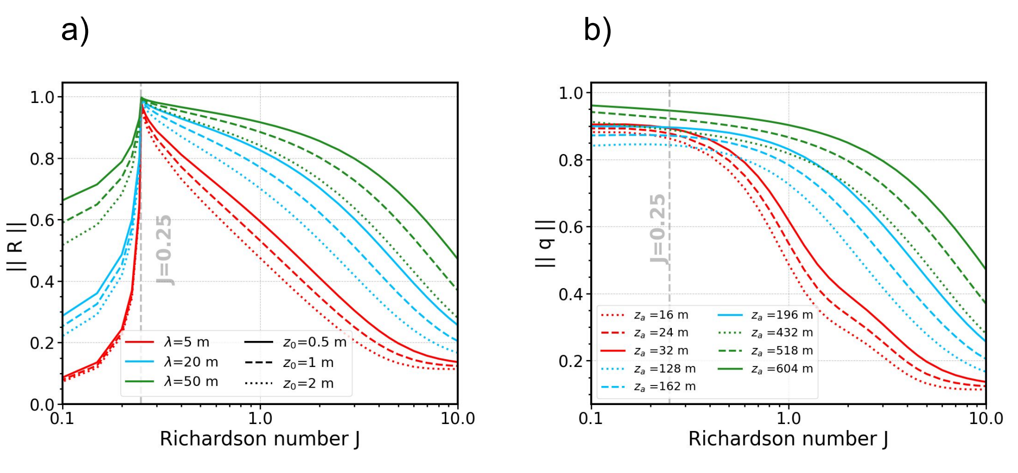

FIGURE 2 Surface reflection coefficient : a) Aloft the inner layer; b) In the far field in the hydrostatic variable shear case with $F = 1$. Also in b) the values of the "critical level depth" z_a are given in place of the λ and z_0 given in a).

Figure 2a) shows the amplitude of the reflection R for different roughness length (z_0) and mixing length (λ) as a function of J and for the dominant wavenumber $k = 1/L = 10^{-3}\mathrm{m}^{-1}$. When $J > 0.25$, we see that this coefficient decreases with stability, which is consistent with the fact that solutions with larger μ oscillate more rapidly in the vertical when J increases and are therefore more absorbed. This behavior is illustrated in Fig. 3: for a given and quite small z_a, the inviscid solution (black curves) oscillates much more when J is large, at least in the region where dissipative effects start to be significant (region arbitrarily placed below $5h_i$ here).

We can also notice that the reflection coefficient decreases with the roughness length, consistently with the fact that enhanced roughness length leads to more dissipation. This has been shown and quantified by Jiang et al. (2006) in a simple model of wave reflection. Quite surprisingly nevertheless, one also sees that absorption decreases (R increases) when the limit value of the mixing length λ increases as if more dissipation results in less absorption. To interpret this, one needs to recall that the oscillatory behaviour in the solutions $\mathbf{w}_{v1}$ and $\mathbf{w}_{v2}$ is more pronounced near the surface when the apparent critical depth is not too large (z_a in Eq. (11)). As shown in table 1, this depth decreases when z_0 increases but increases when λ increases, which explains the absorbing behaviour seen in Fig. 2a. Again, the fact that absorption becomes less sensitive to J when z_a is large is also illustrated by the red curves in Fig. 3: when $z_a = 162$m, the differences in oscillatory behaviour oscillations between $J = 0.3$ and $J = 4$, are not as pronounced when z_a is smaller. Accordingly the decrease in reflection when J increases is therefore less pronounced (compare the dashed blue and red dot curves in Figs. 2). Finally, it is important to notice that $|R|$ is not sensitive to the choice of k because the inner equations we solved in Part I become independent of k when inner varibles are used. This of course stays true in the limit of validity of our analysis, that is when:

$$\lambda < \delta(k) < d. \tag{25}$$

The results for $|R|$ when $J < 0.25$ are more problematic to interpret because in this case $\mathbf{w}_{v1}$ and $\mathbf{w}_{v2}$ in Eq. (23) cannot be associated with downward and upward gravity waves. To circumvent this difficulty one needs to look further aloft for instance where the wind becomes constant in the variable shear case. There, as the two solutions $\mathbf{w}_D$ and $\mathbf{w}_I$ in (18) only represent downward and upward propagating waves when m is imaginary, we make the hydrostastic approximation to ensure that it is always the case (see (20)). With this approximation, the harmonics are no longer trapped and we can analyse the wave reflection in $z \to \infty$ by writing the solution in the outer region under the form,

$$\mathbf{w} = U_p \mathbf{w}_I + D_o \mathbf{w}_D \underbrace{\approx}_{z\to 0} (U_p a_1 + D_o a_3)\,(z+z_a)^{1/2+i\mu} + (U_p a_2 + D_o a_4)\,(z+z_a)^{1/2-i\mu}\,, \tag{26}$$

the matching with the inner solution in being done by neglecting the viscous solutions in (23) that are exponentially small when $z/\delta \to \infty$. This yields the total reflection coefficient,

$$q = \frac{U_p}{D_o} = \frac{a_4 - a_3 R}{a_2 - a_1 R}. \tag{27}$$

As shown in Fig. 2b), when $F = 1$ ($d = \sqrt{J}L$), the amplitude of this coefficient $|q|$ behaves almost as $|R|$ when $J > 0.25$ and becomes near 1 (near total reflection) when $J < 0.25$. Again, as in the outer layer the hydrostatic solutions are such that the a_is do not depend on k and as $|R|$ does not depend on k, $|q|$ does not vary much with k either. There is nevertheless a weak sensitivity: keeping values in the range $0.5/L < k < 2L$ we found that slightly more absorption occurs when k decrease, i.e. when the inner layer h_i get closer from the boundary layer depth d (not shown).

This interpretation that the surface reflection is near 1 when $J < 0.25$ nevertheless has a limit. Indeed, the coefficient q is more than a surface reflection coefficient since partial reflections of the incident wave can occur where the wind curvature is large (around $z = d$ and even in the hydrostatic case because the Scorer parameter varies there). We verified that these partial reflections have small qualitative impacts by making sensitivity tests of our results to the Froude number F (and hence d, not shown). This weak sensitivities to the curvature around d probably follows that the tanh function used to stop the infinite growth with altitude of the boundary layer wind U_v in (9) is very smooth. This tanh profile was chosen in Lott (2007) to minimize these partial reflections. It permits to say with confidence that the amplitude of the hydrostatic approximation of q essentially measures surface reflection.

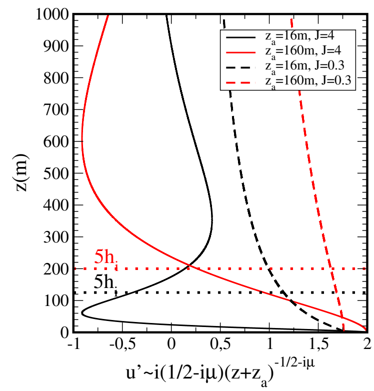

FIGURE 3 Schematic representation of the horizontal velocity field associated with the Booker and Bretherton (1967)'s downward solutions $\mathbf{u}_1 = \frac{i}{k}\,(1/2 - i\mu)\,(z + z_a)^{-1/2-i\mu}$ for z_a=16m, 162m, and $J = 0.3, 4$. Only the real part is shown for conciseness.

5 | TRAPPED LEE WAVE DEVELOPMENT

To determine the manner in which the trapped waves change as flow stability and dissipations change, we next use the model presented in Part I, and where the mountain is represented by a 2D gaussian ridge of characteristic horizontal length L:

$$h(x) = He^{-\frac{x^2}{2L^2}} \tag{28}$$

where H is the maximum mountain height. The ratio $S = H/L$ is fixed to 0.2 keeping $L = 1$ km. With these parameters, the gaussian mountain forces harmonics with dominant wavenumber around $k = 1\text{km}^{-1}$. In this model where disturbances come from the surface, and in contrast with the previous section, we recall that each harmonics $\mathbf{w}(k, z)$ varies in the vertical and when $z >> d$ according to

$$e^{-m(z+z_a)} \text{ where } m = \begin{cases} -i\sqrt{F^{-2}L^{-2} - k^2} & \text{for} \quad k < k_c = (FL)^{-1} \\ \sqrt{k^2 - F^{-2}L^{-2}} & \text{for} \quad k > k_c \end{cases} \tag{29}$$

where k_c is the cutoff wavenumber separating trapped and freely propagating harmonics.

5.1 | Wave field

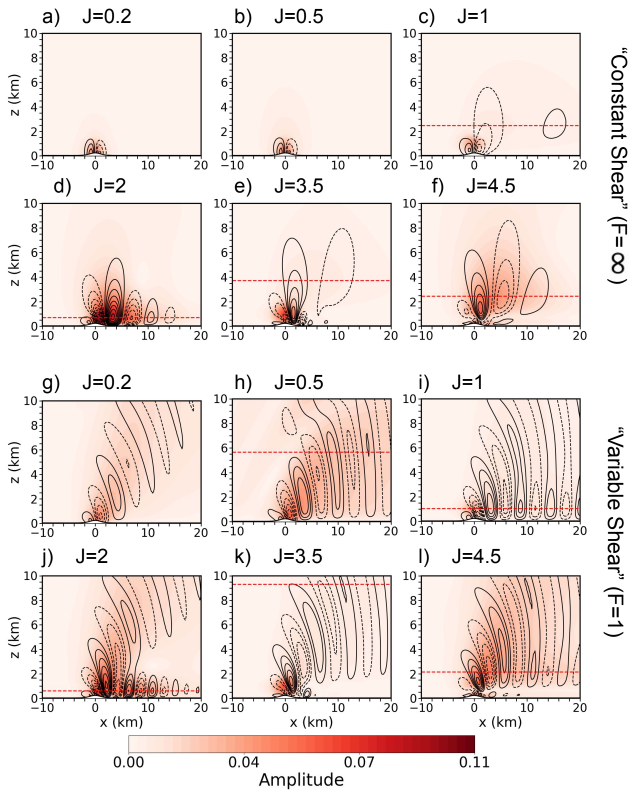

FIGURE 4 Vertical velocity fields $w(x, z)$ for a roughness length $z_0 = 1$ m and a mixing length $\lambda = 20$ m ($z_a = 162$ m). The 6 top figures are for the "constant shear case" ($F = \infty$), and the 6 bottom figures are for the "variable shear case" with $F = 1$. Between panels in each two case only varies the Richardson number J. In all panels, the contour interval is fixed to 0.01 m.s^{-1} and the color represents the amplitude of w. The red dashed lines give the altitude where the characteristics of the dominant trapped waves are extracted (see section 5.2).

The vertical velocity fields are plotted in Figure 4 for different values of the Richardson number J and for $z_0 = 1$ m and $\lambda = 20$ m. The 6 top panels show the wave field for the constant shear case, i.e. for $F = \infty$, and thus $m = k$ (see

(29)). The wave fields obtained with the variable shear ($F = 1$) are sketched in the 6 bottom panels.

When $F = \infty$ the 6 top panels show that the wave field decreases rapidly with altitude, as a result of the presence of turning heights (and hence real m's) for each wavenumber. For small J, these turning heights $h_t(k)$ in (2) are close to the surface compared to the horizontal scale (i.e. $h_t(1/L)/L < 1$), whereas they are quite far for large J. Accordingly and for small J the trapping region is too narrow vertically compared to the horizontal scale of the waves and trapped modes do not emerge as Figs. 4a), 4b) show. Some signal downstream the mountain start to appear at $J = 1$ (Fig. 4c)), downstream decaying trapped waves dominating the response for $J > 1$. For $J = 2$, we observe one dominant mode confined at low level and substantially decaying downstream (Fig. 4d)) whereas for $J = 3.5$ two modes coexist (Fig. 4e)): the longest mode appears at higher altitude than for smaller J whereas the second much shorter mode emerges from the lower part of the flow, immediatly downstream the mountain and confined near the surface. Note that for $J = 4.5$ this low level mode is extremely attenuated consistent with the fact that the surface is strongly absorbing. The fact that the responses present multiple modes and that the dominant one is confined near the surface for small J and developing higher for larger J's are studied further in section 5.2.

When $F = 1$, the six lowest panels in Fig. 4 show that an important feature of the wave field arises from the harmonics that do not encounter a turning altitude (i.e. for which we have $k < k_c$). These harmonics are free to propagate in the far-field and combine to form a system of upward propagating waves. When $J = 0.2$, in Fig. 4g) this far-field component dominates aloft, there is very small downstream signal at low level (somehow reminiscent of the very small low-level signal in the constant shear case in Fig. 4a)). As when $F = \infty$ in Fig. 4a) the turning levels are too close from the surface for trapped modes to emerge. Low level trapped waves become more substantial when J increases (4h), 4i), 4j)), due to the fact that the ducting region thickens. Interestingly, for $J = 0.5$, the trapped wave merges with the system of upward propagating waves above the mountain. As we shall see in the next section, this occurs because the dominant trapped mode that first arise when J increases have horizontal wavenumber near the "cut-off" value separating trapped and propagating harmonics (e.g. $k = 1/(FL)$, see (19)). As J increases further, the wave signal near the surface becomes distinct from that in the far field . It also decays downstream faster when J increases from $J = 1$ to $J = 2$ (see Fig. 4i) and 4j) below $z = 2$km). This low level signal becomes very small for $J = 3.5$ (Fig. 4k)), we presume that in this case the surface absorption is too large for low level trapped modes to develop downstream. For even larger J in Fig. 4l), and similarly to the case with $F = \infty$ in Fig. 4j) a second mode emerges above the first one, which is no longer confined near the surface but quite significant and much less attenuated.

5.2 | Trapped waves

The downstream evolution of dissipated trapped mountain waves can be characterized using a description in term of wavepacket of complex wavenumber (Teixeira and Argaín (2022)). To follow this approach in a diagnostic context we will use surrogates of the form

$$\mathbf{w}_S = A e^{ikx - \alpha x} \tag{30}$$

where the amplitude A is a complex, α denotes the downstream decay rate and k the horizontal wavenumber. To evaluate α and k, we minimize the misfit between $\mathbf{w}(x, z_{\max})$ and the surrogate, where $z_{\max}$ is the altitude at which the trapped waves present a relative maximum in the amplitude of $\mathbf{w}$. This altitude is obtained by averaging between 5km $< x <$ 40km the envelope of w obtained by combining w and its Hilbert transform in the horizontal direction (see figure 5a)). The parameters α and k are finally estimated by minimizing the square distance between $\mathbf{w}$ and $\mathbf{w}_S$ at $z_{\max}$, Fig. 5b) illustrate the obtained values when $J = 2$ and $z_a = 162$m ($\lambda = 20$m $z_0 = 1$m).

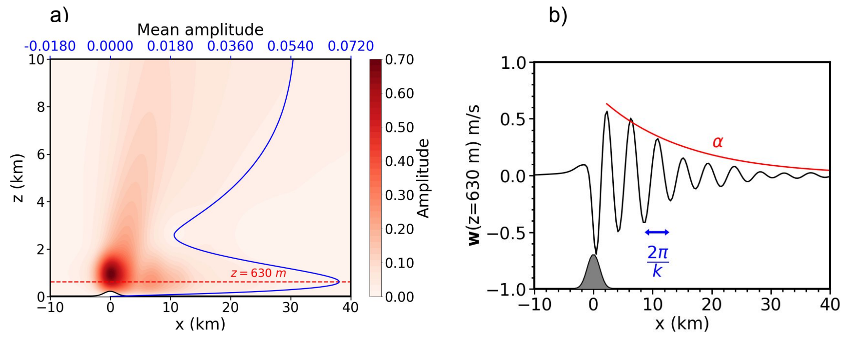

FIGURE 5 Extraction of α and k for $z_a = 162$ m and $J = 2$. (a) Amplitude of the vertical velocity perturbations obtained by combining w and its Hilbert transform (colors), amplitude averaged between $x = 5$ km and $x = 40$ km (blue) and altitude z_{max} of the corresponding maximum amplitude (red). (b) vertical velocity w at z_{max} and mountain (grey).

Figure 6 shows how the decay rate α and the wavenumber k are affected by the Richardson number J and the critical level depth z_a. For a fixed $z_a = 162m$, the decay rate in Fig. 6a) tends to increase with J consistent with the fact that the waves are more absorbed by the surface (see Fig. 2b)). Nevertheless the approach for tracking the low level wave properties produces a jump for $k(J)$ and $\alpha(J)$ as J increases. This behaviour is related to the co-existence of two damped modes and indeed, when the transition occurs, the pair (k, α) that minimizes $\mathbf{w} - \mathbf{w}_S$ captures the wave that is less absorbed. In general, the less absorbed wave is that which is less confined at low level. This upper level trapped wave is clearly apparent when $J = 4.5$ in both the constant shear and variable shear case in Figs. 4f) and 4l) respectively. This is in contrast with the cases at lower J where the lower level trapped wave is dominant (for $J = 2$ see Figs. 4d) and 4l)). Note that after the jump in α, the decay rate continues to increase when J increases, but the increase is less pronounced because for such waves the interaction with the surface is not as strong. Note also that the decay rates are more pronounced in the constant shear cases ($F = \infty$) then when $F = 1$, again because the waves are more confined and return faster to the surface where they are absorbed. Note also that in the cases with $F = \infty$ the dominant modes often have smaller k's than in the variable shear case, which simply follows that waves with $k < 1/L$ cannot be trapped when $F = 1$. Similarly, Figs. 6c), 6d) show α and k respectively and as functions of z_a for fixed values of J. It is interesting to emphasize here that for a given J, the damping rate is larger for small z_a, as a result of more dissipation in the lower layer. This is consistent with the results of section 4 showing that waves are more absorbed when the critical level is near below the surface (z_a small).

Some prediction of the preferred wavenumbers can also be obtained using the reflection coefficient resonances, that is from $|q(k)|$ in (27) but without making the hydrostatic approximation: for trapped waves and when $|q(k)|$ presents a maximum when k varies beyond the cut-off wavenumber ($k_c = 1/(FL)$ see (19)), the exponentially decaying inviscid solution ($\mathbf{w}_I$ in (18a)) largely dominates the exponentially growing one ($\mathbf{w}_D$ in (18a)). As the Richardson number at the surface $Ri(z = 0) = 0$ we follow Lott (2007) and assume that the resonance that corresponds to trapped waves are those occurring near the cut-off wavenumber ($k_c = 0$ in the constant shear case and $k_c = 1\text{km}^{-1}$ in the variable shear case). In the following, we therefore only keep the first trapped wave modes with values of k larger than the cut-off wavenumber and giving maxima in $|q(k)|$. Figure 6b) shows that in the constant shear case there is good agreement between the first two modes obtained from the resonances of $|q|$ and the mode captured using the model. In this case when multiple modes are possible, the diagnostics from the model presented before capture the mode with smaller wavenumber k since it is less confined near the surface. In the variable shear case, we find some correspondence as well, at least when $J < 3$ and for the first maximum of $|q|$, but proliferation of adjacent resonances in $|q|$ when J is larger make the correspondence less straightforward (not shown).

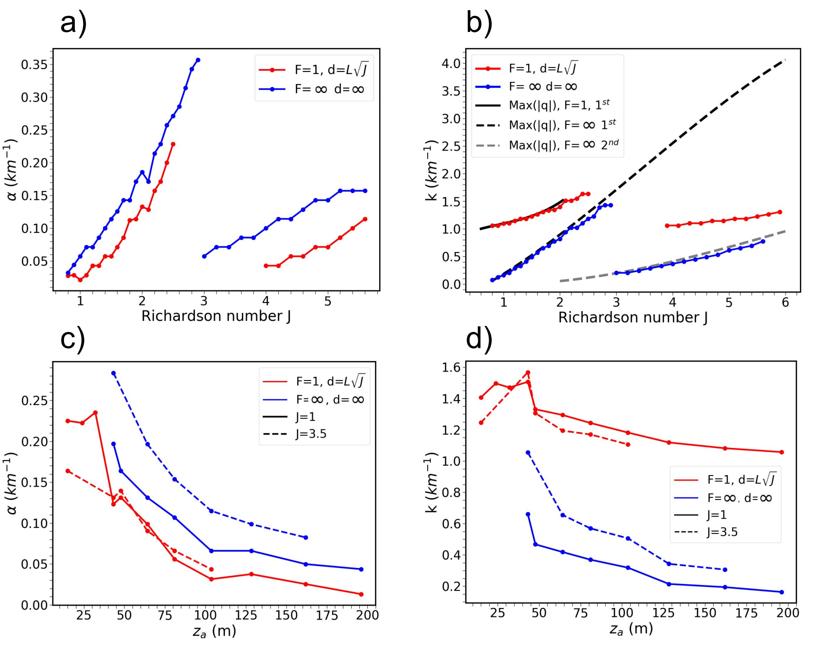

FIGURE 6 Spatial decay rate α (a,c) and wavenumber k (b,d) extracted from the model. (a,b) for z_a = 162m and as function of the Richardson number J; (c,d) For two values of J and as a function of the critical level depth z_a. The thin solid lines with dots give the results obtained from the minimization problem when the Froude number $F = \infty$ (blue) and $F = 1$ (red). The thick solid lines in shades of grey in b) give the first two modes from the maxima of $|q(k)|$, and for k increasing beyond $k_c = 1/(FL)$, i.e. $k_c = 0$ when $F = \infty$ and $k_c = 1\text{km}^{-1}$ when $F = 1$

5.3 | Agreement with the inviscid theory

Figure 6b)a and 6d) also shows that the dominant wavenumber of the trapped modes have a tendency to increase when J increases and to decrease when z_a increases. To a large extent this is more related to inviscid dynamics than to dissipations. To establish this, we next ask ourselves if the much simpler inviscid theories developed in the past stay valid. For this purpose, we consider solutions to the inviscid Taylor Goldstein equation taking for incident flow (17). For such flow where the surface "log"-layer is absent, the potentially resonant inviscid solutions for $F = \infty$ and $F = 1$ are given by the $\mathbf{w}_I$ in (33a) and (36a)) respectively and for wavenumbers k such that $\mathbf{w}_I(k, z = 0) = 0$.

Figure 7a) and 7b) plots the wavenumbers extracted from the full dissipative theories as a function of the wavenumbers predicted by the inviscid theory and in the constant shear case ($F = 0$). In these two figures all the parameters of interest are changed (z_0, λ, J) but we managed to distinguish two quite separate regimes. On the left panel (Fig. 7a),

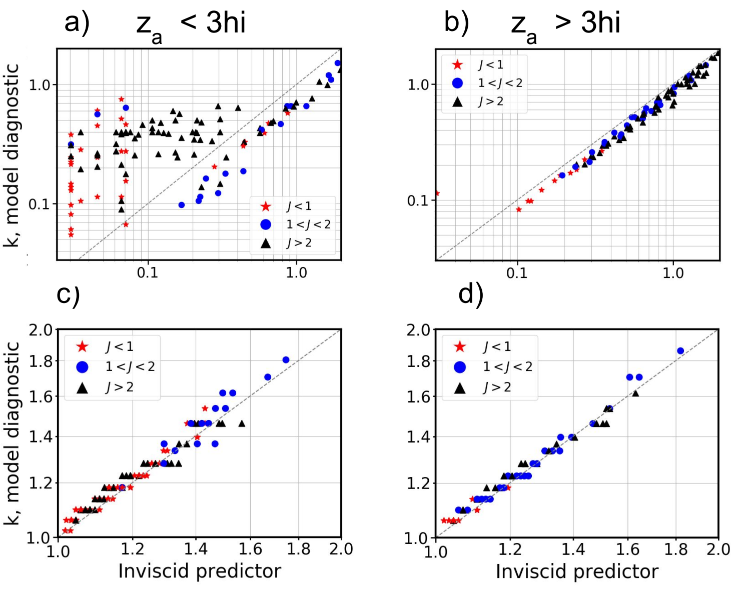

FIGURE 7 Wavenumbers evaluated with the full dissipative theories as a function of the wavenumbers predicted by the inviscid theory. The upper panels show the constant shear cases $d = \infty$, the lower panels show the variable shear case, $d = \sqrt{J}L$. On the left (right) are cases with critical level near (far) below the surface (i.e. $z_a < 3h_i$ and $z_a > 3h_i$ respectively).

the depth of the critical level $z_a < 3h_i$ on the right (Fig. 7b) $z_a > 3h_i$. It therefore shows that the inviscid theory is quite right when the critical level is far below the surface compared to the inner layer depth, but fails when it is quite near. The same comparison in the variable shear case ($F = 1$) in Figs. 7c) and 7c) deliver about the same message except maybe that the inviscid predictor is more accurate than in the constant shear case since the inviscid predictor work quite well when z_a is quite near below the surface (compare Figs. 7a) and 7c)).

6 | SUMMARY

The purpose of this paper is to analyse the trapped waves that can occur when a turbulent boundary layer interacts with a low mountain ridge. We use for that a linear theory developed in a companion paper (Part I), and where turbulence is represented by a viscosity which amplitude varies according to the mixing length theory. We are aware that such a theory oversimplifies the interaction between turbulence and the obstacle, for instance neglecting the impact of the disturbance on the mixing length, or the dependence of the mixing length on flow stability. It also neglects that the disturbances produce turbulence in the outer part of the flow, i.e. that turbulence and dissipative effects penetrate in the outer layer. Much more fundamentally it also neglects that at the horizontal scales we analyse the turbulent eddies can backscatter on the large scale, effect that is entirely absent when representing turbulence with eddy viscosity (see Sun et al. (2015)). This being said, we believe that our theory stays more realistic than the theories developed so far to describe the interaction between mountains and boundary layers (Smith et al., 2002; Lott et al., 2020a). Also, the closure we analyse is somehow representative of the turbulence closures adopted in the atmospheric mesoscale models that are used to do large-eddy simulations in mountainous areas (Doyle et al., 2011). In this respect, our theory could help interpreting what occurs in these models.

The first message is that near the surface the undisturbed boundary layer flow has null Richardson number by construction, and is less absorptive than in the constant viscosity case analysed for instance in Lott (2007) (compare Figs. 2a) and 2b) with and Figs. 2 and 3 in Lott (2007) respectively). We interpret this by the fact that the surface critical level absorption at work in Lott (2007) is less effective because the critical level migrates below the surface in the cases considered here. As an illustration, we find that absorptions only compare to those in Lott (2007) when the critical level depth z_a is small. We also find that this depth is large and absorption is small when the limit value of the mixing length is large, as if more dissipation resulted in less absorption! This is because at fixed roughness length, increasing λ yields a larger critical level depth z_a. Due to the central role of this parameter, we could suggest to diagnose it in practice, for instance by fitting a linear function to the boundary layer winds above the surface layer and identify at which depth this function is null below the surface. We also found that absorption increase with the Richardson number value of the background flow in the boundary layer, and this occurs because more oscillatory behaviours near the surface result in more absorption, as in Lott (2007).

We next relate the absorptive properties of the inner layer to the decay rate of the trapped waves downstream and found that they are indeed well related. We also found that the trapped waves often has horizontal wavenumbers quite near the cut-off value $\sqrt{N}(\infty)/U(\infty)$, a behaviour we also found when the Richardson number at the surface is null in Lott (2007), as is always the case here. For quite large Richardson numbers aloft the inner layer J, which are cases where the surface absorption is strong, the analysis also reveals the presence of gravity waves propagating downstream. Their decay rate is quite small despite the fact that the surface is supposedly absorbing them substantially. This new class of waves are characterized by the fact that they have small amplitude near the surface, and large amplitude at the boundary layer height and above. As these waves appear when J is quite large, the fact that the ducting region depth becomes quite large is presumably central. Indeed they are reflected back toward the surface at turning points much higher than when J is small and we can presume that they reach the surface at much larger distance downstream than when J is smaller. These waves are therefore absorbed at the surface at a much longer distance from the obstacle than those that stay confined near the surface.

We have also tried to test if the more classical inviscid theories can still be applied to predict trapped waves, and when considering boundary layer flow without surface "log"-layer. We found that it is general the case, at least for predicting the horizontal wavenumbers. Some discrepancies can nevertheless appear when dissipations are large, which in our case means that the critical level depth z_a is small.

Data availability statement

The theoretical model used to support the findings of this study is available from the corresponding author upon request.

A | OUTER SOLUTIONS IN THE CONSTANT SHEAR CASE

In the outer region, the solutions are the inviscid solutions of the Taylor Goldstein equation,

$$\frac{d^2\mathbf{w}}{dz^2} + \left(\frac{N^2}{U^2} - \frac{U_{zz}}{U} - k^2\right)\mathbf{w} = 0 \tag{31}$$

which in the constant shear case approximates into the Bessel's equation

$$\frac{d^2\mathbf{w}}{dz^2} + \left(\frac{J}{(z+z_a)^2} - k^2\right) w = 0. \tag{32}$$

A solution in term of Hankel function and for exponentially decaying disturbances in the farfield is developed in Lott et al. (2020b), it is extended here to include exponentially growing solutions, and writes when $k > 0$:

$$\mathbf{w}_I = i\sqrt{\frac{\pi k(z+z_a)}{2}}e^{-\mu\pi/2}H^{(1)}_{i\mu}\left(ik(z+z_a)\right) \underbrace{\approx}_{z\to\infty} e^{-k(z+z_a)}, \tag{33a}$$

$$\mathbf{w}_D = \sqrt{\frac{\pi k(z+z_a)}{2}}e^{+\mu\pi/2}H^{(2)}_{i\mu}\left(ik(z+z_a)\right) \underbrace{\approx}_{z\to\infty} e^{+k(z+z_a)}, \tag{33b}$$

where μ is given in (19). In the far field, the asymptotic behaviours of (33) are as in (18) keeping in mind that $m = k$ in (19) when $d = \infty$. Near the surface, (33) are as (18) as well (see 9.1.3, 9.1.4, and 9.1.7 in AS), and by taking,

$$a_1 = \frac{-i\sqrt{\pi}}{\sinh(\mu\pi)\Gamma(1-i\mu)}\left(\frac{k}{2}\right)^{1/2-i\mu}, \quad a_2 = a_1^*, \tag{34a}$$

$$a_3 = \frac{\sqrt{\pi}e^{\mu\pi}}{\sinh(\mu\pi)\Gamma(1-i\mu)}\left(\frac{k}{2}\right)^{1/2-i\mu}, \quad a_4 = -\frac{\sqrt{\pi}e^{-\mu\pi}}{\sinh(\mu\pi)\Gamma(1+i\mu)}\left(\frac{k}{2}\right)^{1/2+i\mu}. \tag{34b}$$

B | OUTER SOLUTIONS IN THE VARIABLE SHEAR CASE

In the variable shear case $d \neq \infty$, the solution for upward propagating waves was developed in the appendix of Soufflet et al. (2022) and the calculation is extended again here to include downward propagating waves. More precisely, and when taking $r = \tanh^2((z+z_a)/d)$, the Taylor-Goldstein equation (31) becomes Eq. A1 in Soufflet et al. (2022)) it is there transformed into an hypergeometric equation when accounting for the change of variable:

$$\mathbf{w} = r^{\frac{1}{4}+i\frac{\mu}{2}}(1-r)^{-\frac{md}{2}}W, \tag{35}$$

where μ and m are in (19) again (see also Eq. 8 in Lott et al. (1992)). Two inviscid solutions are :

$$\mathbf{w}_I = 2^{-md} r^{1/4+i\mu/2}(1-r)^{-md/2} W_{2(1)} \underbrace{\approx}_{z\to\infty} e^{-m(z+z_a)} \tag{36a}$$

$$\mathbf{w}_D = 2^{+md} r^{1/4+i\mu/2}(1-r)^{-md/2} W_{1(1)} \underbrace{\approx}_{z\to\infty} e^{+m(z+z_a)} \tag{36b}$$

And where $\mathbf{w}_I$ and $\mathbf{w}_D$ are unique amplitude waves propagating upward and downward respectively when m is imaginary. The solutions $W_{1(1)}$ and $W_{2(1)}$ are expressed with the hypergeometric function F:

$$W_{1(1)} = r^{-i\mu} F\left(-\frac{1}{4} - \frac{i\mu}{2} - \frac{md}{2}, \frac{5}{4} - \frac{i\mu}{2} - \frac{md}{2}; 1-md; 1-r\right) \tag{37a}$$

$$W_{2(1)} = (1-r)^{md} F\left(\frac{i\mu}{2} + \frac{5}{4} + \frac{md}{2}, \frac{i\mu}{2} - \frac{1}{4} + \frac{md}{2}; 1+md; 1-r\right) \tag{37b}$$

Then, to evaluate the solution near the surface, we use relations (15.3.6) given in Abramowitz and Stegun (1964), to link $W_{1(1)}, W_{2(1)}, W_{1(0)}, W_{2(0)}$ with the help of A_1, A_2, A_3, A_4 calculated in the appendix of Soufflet et al. (2022):

$$W_{1(0)} = A_1 W_{1(1)} + A_3 W_{2(1)}, \qquad W_{2(0)} = A_2 W_{1(1)} + A_4 W_{2(1)}. \tag{38}$$

That leads to a total solution (combination of upward and downward propagating waves),

$$D_o \mathbf{w}_D + U_p \mathbf{w}_I = r^{\alpha_1}(1-r)^{\gamma_1}(D_o(a_4 \mathbf{w}_{1(0)} + a_3 \mathbf{w}_{2(0)}) + U_p(a_2 \mathbf{w}_{1(0)} + a_1 \mathbf{w}_{2(0)})), \tag{39}$$

where $\mathbf{w}_{1(0)}$ ($\mathbf{w}_{2(0)}$) is related to $W_{1(0)}$ ($W_{2(0)}$) by using Eq. 35 and

$$a_j = \begin{cases} (-1)^{j-1} \dfrac{2^{-md} A_j}{A_1 A_4 - A_3 A_2} d^{-1/2+(-1)^{j-1} i\mu} & \text{for j=1,2} \\ (-1)^{j} \dfrac{2^{md} A_j}{A_1 A_4 - A_3 A_2} d^{-1/2+(-1)^{j-1} i\mu} & \text{for j=3,4} \end{cases} \tag{40}$$

references

Abramowitz, M. and Stegun, I. A. (1964) *Handbook of mathematical functions: with formulas, graphs, and mathematical tables*, vol. 55. Courier Corporation.

Belcher, S. E., Newley, T. M. J. and Hunt, J. C. R. (1993) The drag on an undulating surface induced by the flow of a turbulent boundary layer. *Journal of Fluid Mechanics*, **249**, 557–596.

Belcher, S. E. and Wood, N. (1996) Form and wave drag due to stably stratified turbulent flow over low ridges. *Quart. J. Roy. Meteor. Soc.*, **122**, 863–902.

Booker, J. R. and Bretherton, F. P. (1967) The critical layer for internal gravity waves in a shear flow. *J. Fluid Mech.*, **27**, 102–109.

Bougeault, P., Binder, P., Buzzi, A., Dirks, R., Houze, R., Kuettner, J., Smith, R. B., Steinacker, R. and Volkert, H. (2001) The map special observing period. *Bulletin of the American Meteorological Society*, **82**, 433–462.

Doyle, J. D., Gaberšek, S., Jiang, Q., Bernardet, L., Brown, J. M., Dörnbrack, A., Filaus, E., Grubišić, V., Kirshbaum, D. J., Knoth, O., Koch, S., Schmidli, J., Stiperski, I., Vosper, S. and Zhong, S. (2011) An intercomparison of t-rex mountain-wave simulations and implications for mesoscale predictability. *Monthly Weather Review*, **139**, 2811 – 2831.

Drazin, P. G. (1958) The stability of a shear layer in an unbounded heterogeneous inviscid fluid. *J. Fluid Mech.*, **4**, 214–224.

Durran, D. R. (1986) Another look at downslope windstorms. part i: The development of analogs to supercritical flow in an infinitely deep, continuously stratified fluid. *Journal of Atmospheric Sciences*, **43**, 2527 – 2543. URL: `https://journals.ametsoc.org/view/journals/atsc/43/21/1520-0469_1986_043_2527_aladwp_2_0_co_2.xml`.

Georgelin, M., Richard, E., Petitdidier, M. and Druilhet, A. (1994) Impact of subgrid-scale orography parameterization on the simulation of orographic flows. *Monthly Weather Review*, **122**, 1509 – 1522. URL: `https://journals.ametsoc.org/view/journals/mwre/122/7/1520-0493_1994_122_1509_iossop_2_0_co_2.xml`.

Goger, B., Rotach, M. W., Gohm, A., Stiperski, I., Fuhrer, O. and de Morsier, G. (2019) A new horizontal length scale for a three-dimensional turbulence parameterization in mesoscale atmospheric modeling over highly complex terrain. *Journal of Applied Meteorology and Climatology*, **58**, 2087 – 2102.

Howard, L. N. (1961) Note on a paper of john w miles. *J. Fluid Mech.*, **10**, 509–512.

Hunt, J. C. R., Richards, K. J. and Brighton, P. W. M. (1988) Stably stratified shear flow over low hills. *Quart. J. Roy. Meteor. Soc.*, **114**, 859–886.

Jackson, P. S. and Hunt, J. C. R. (1975) Turbulent wind flow over low hill. *Quart. J. Roy. Meteor. Soc.*, **101**, 929–955.

Jansing, L., Papritz, L., Dürr, B., Gerstgrasser, D. and Sprenger, M. (2022) Classification of alpine south foehn based on 5 years of kilometre-scale analysis data. *Weather and Climate Dynamics*, **3**, 1113–1138.

Jiang, Q., Doyle, J. D. and Smith, R. B. (2006) Interaction between trapped waves and boundary layers. *J. Atmos. Sci.*, **63**, 617–633.

Keller, T. L. (1994) Implications of the hydrostatic assumption on atmospheric gravity waves. *Journal of the atmospheric sciences*, **51**, 1915–1929.

Lehner, M. and Rotach, M. W. (2018) Current challenges in understanding and predicting transport and exchange in the atmosphere over mountainous terrain. *Atmosphere*, **9**. URL: `https://www.mdpi.com/2073-4433/9/7/276`.

Lott, F. (2007) The reflection of a stationary gravity wave by a viscous boundary layer. *J. Atmos. Sci.*, **139**, 3363–3371.

Lott, F., Beljaars, A., Pauget, L. and Deremble, B. (2023) Neutral and stratified turbulent boundary layer flow over low mountains. *Quart. J. Roy. Meteor. Soc.* URL: `https://doi.org/10.1002/qj.4591`.

Lott, F., Deremble, B. and Soufflet, C. (2020a) Mountain waves produced by a stratified boundary layer flow. part i: Hydrostatic case. *Journal of the Atmospheric Sciences*, **77**, 1683–1697.

— (2020b) Mountain waves produced by a stratified shear flow with a boundary layer. part ii: Form drag, wave drag, and transition from downstream sheltering to upstream blocking. *Journal of the Atmospheric Sciences*, **78**, 1683–1697. URL: https://doi.org/10.1175/JAS-D-20-0144.1.

Lott, F., Kelder, H. and Teitelbaum, H. (1992) A transition from Kelvin–Helmholtz instabilities to propagating wave instabilities. *Physics of Fluids A: Fluid Dynamics*, **4**, 1990–1997.

Miles, J. W. (1961) On the stability of heterogeneous shear flow. *J. Fluid. Mech.*, **10**, 496–508.

Miller, P. P. and Durran, D. R. (1991) On the sensitivity of downslope windstorms to the asymmetry of the mountain profile. *Journal of Atmospheric Sciences*, **48**, 1457 – 1473. URL: https://journals.ametsoc.org/view/journals/atsc/48/12/1520-0469_1991_048_1457_otsodw_2_0_co_2.xml.

Richard, E., Mascart, P. and Nickerson, E. C. (1989) The role of surface friction in downslope windstorms. *J. Appl. Meteor.*, **28**, 241–251.

Sachsperger, J., Serafin, S., Grubišić, V., I, I. S. and Paci, A. (2017) The amplitude of lee waves on the boundary-layer inversion. *Quart. J. Roy. Meteor. Soc.*, **143**, 27–36.

Scorer, R. S. (1949) Theory of waves in the lee of mountains. *Quart. J. Roy. Meteor. Soc.*, **75**, 41–56.

Serafin, S., Adler, B., Cuxart, J., De Wekker, S. F. J., Gohm, A., Grisogono, B., Kalthoff, N., Kirshbaum, D. J., Rotach, M. W., Schmidli, J., Stiperski, I., Vecenaj, Z. and Zardi, D. (2018) Exchange processes in the atmospheric boundary layer over mountainous terrain. *Atmosphere*, **9**.

Smith, R. B., Jiang, Q. and Doyle, J. D. (2006) A theory of gravity wave absorption by a boundary layer. *J. Atmos. Sci.*, **63**, 774-–781.

Smith, R. B., Skubis, S., Doyle, J. D., Broad, A. S., Kiemle, C. and Volkert, H. (2002) Mountain waves over the mont blanc: Influence of a stagnant boundary layer. *J. Atmos. Sci.*, **59**, 2073–2092.

Soufflet, C., Lott, F. and Deremble, B. (2022) Mountain waves produced by a stratified shear flow with a boundary layer. part iii: Trapped lee waves and horizontal momentum transport. *Journal of the Atmospheric Sciences*, **79**, 1601 – 1614.

Sun, J., Nappo, C. J., Mahrt, L., Belušić, D., Grisogono, B., Stauffer, D. R., Pulido, M., Staquet, C., Jiang, Q., Pouquet, A., Yagüe, C., Galperin, B., Smith, R. B., Finnigan, J. J., Mayor, S. D., Svensson, G., Grachev, A. A. and Neff, W. D. (2015) Review of wave-turbulence interactions in the stable atmospheric boundary layer. *Reviews of Geophysics*, **53**, 956–993.

Teixeira, M. A. C. and Argaín, J. L. (2022) The drag exerted by weakly dissipative trapped lee waves on the atmosphere: Application to scorer's two-layer model. *Quarterly Journal of the Royal Meteorological Society*, **148**, 3211–3230.

Teixeira, M. A. C., Argaín, J. L. and Miranda, P. M. A. (2013) Drag produced by trapped lee waves and propagating mountain waves in a two-layer atmosphere. *Quarterly Journal of the Royal Meteorological Society*, **139**, 964–981. URL: https://rmets.onlinelibrary.wiley.com/doi/abs/10.1002/qj.2008.

Tian, Y., Duarte, J. Q. and Schmidli, J. (2023) A station-based evaluation of near-surface south foehn evolution in cosmo-1. *Quarterly Journal of the Royal Meteorological Society*, **150**, 290–317.

Tsiringakis, A., Steeneveld, G. J. and Holtslag, A. A. M. (2017) Small-scale orographic gravity wave drag in stable boundary layers and its impact on synoptic systems and near-surface meteorology. *Quarterly Journal of the Royal Meteorological Society*, **143**, 1504–1516. URL: https://rmets.onlinelibrary.wiley.com/doi/abs/10.1002/qj.3021.

Vosper, S. B. (2004) Inversion effects on mountain lee waves. *Quarterly Journal of the Royal Meteorological Society*, **130**, 1723–1748. URL: https://rmets.onlinelibrary.wiley.com/doi/abs/10.1256/qj.03.63.

Vosper, S. B., Ross, A. N., Renfrew, I. A., Sheridan, P., Elvidge, A. D. and Grubišić, V. (2018) Current challenges in orographic flow dynamics: Turbulent exchange due to low-level gravity-wave processes. *Atmosphere*, **9**. URL: https://www.mdpi.com/2073-4433/9/9/361.

Weng, W., Chan, L., Taylor, P. and Xu, D. (1997) Modelling stably stratified boundary-layer flow over low hills. *Quarterly Journal of the Royal Meteorological Society*, **123**, 1841–1866.

Wurtele, M. G., Sharman, R. D. and Datta, A. (1996) Atmospheric lee waves. *Annual Review of Fluid Mechanics*, **28**, 429–476.

Yu, C. L. and Teixeira, M. A. C. (2014) Impact of non-hydrostatic effects and trapped lee waves on mountain wave drag in directionally sheared flow. *Quarterly Journal of the Royal Meteorological Society*, **141**, 1572–1585.